

# Computational Assignment of Tantalum-related Strong Absorption Peaks in the Infrared Spectrum of Potassium Heptafluorotantalate

Yi-Ning Li, Qing Guo, Si-Cheng Liu, Xiao-Yan Liu, Yan Jiang, Yi Yin, and Peng Zhang\*

Cite This: *ACS Omega* 2024, 9, 988–993

Read Online

ACCESS |



Metrics &amp; More

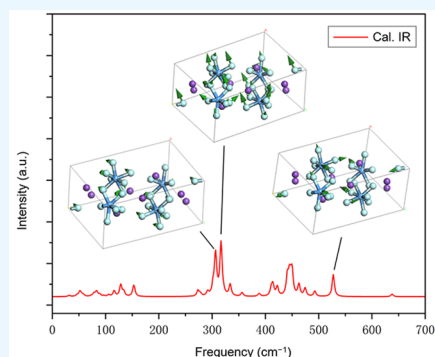


Article Recommendations



Supporting Information

**ABSTRACT:** Tantalum (Ta) is a valuable and rare metal that is extensively used in the production of implant materials and high-performance capacitors. However, a convenient and effective method for the separation of Ta from other compounds has yet to be developed. On the basis of first-principle density functional theory (DFT), we simulated the vibrational spectrum of potassium heptafluorotantalate ( $K_2TaF_7$ ). By performing a dynamics analysis of vibrational modes, we assigned peaks in infrared (IR) absorption and Raman scattering spectra to their corresponding vibrations. We focused on the strong IR absorption peaks of Ta-related vibrational modes in  $K_2TaF_7$  and concluded that three observed IR absorption peaks, at 285, 315, and 530  $cm^{-1}$ , are good candidates. Provided with high power radiation at these three frequencies (at about 8.55, 9.45, and 15.9 THz), the good efficiency of photon–phonon resonance absorption will facilitate Ta separation from a compound.



## I. INTRODUCTION

Tantalum (Ta) is an expensive and rare metal with remarkable properties, such as a high melting point; excellent chemical stability and cold working performance; and strong resistance to liquid metal, acid, and alkali corrosion.<sup>1</sup> Thus, Ta is an important metal that is widely used in high-technology industries, such as superconductor,<sup>2</sup> aircraft,<sup>3</sup> and atomic energy industries.<sup>4</sup> In addition, Ta is frequently employed to manufacture electromagnetic components and military hardware,<sup>5</sup> and Ta powder is typically used to manufacture capacitors.<sup>6</sup> Ta also has excellent biocompatibility and does not cause inflammatory reactions in human cells.<sup>7</sup> Moreover, Ta naturally forms a stable passive oxide layer, which provides protection against in vivo corrosion.<sup>7</sup> Because of its exceptional chemical and biomedical properties,<sup>8–10</sup> Ta is recognized as a next-generation implant material.<sup>11</sup> Therefore, obtaining high-purity Ta is emerging as an essential goal for various industries and applications.

Thermal reduction<sup>12–15</sup> and molten-salt electrodeposition from molten salt<sup>16,17</sup> are the two main methods used to separate Ta from other compounds. Thermal reduction involves the frequent use of heat, oxygen reduction, and other high-temperature treatments during production and application processes, resulting in significant energy usage. Moreover, the high reactant concentrations of electrodeposition employed result in the production of Ta powders that exhibit insufficiently high specific surface areas when they are used in melts,<sup>18</sup> which means that such powders lack the required high specific capacities. The reduction of reactants in melts with a high concentration (>90 wt %) of diluent salt can lead to a significant increase in the specific surface area.<sup>19</sup>

However, this results in a decrease in process productivity, and when the resulting Ta powder is washed, considerable volumes of fluorine-containing reject solutions are formed.<sup>20</sup> In addition, the ionic liquid used in the molten salt electrodeposition process has a high production cost. Moreover, due to their high melting points, molten salts demand high working temperatures, which greatly affects energy expenditures and material compatibilities.<sup>21</sup> Thus, an efficient and energy-saving method for the separation of Ta from other compounds must be developed to facilitate the preparation of a high-purity Ta powder with a high specific capacity.

Many spectroscopy studies have focused on potassium heptafluorotantalate ( $K_2TaF_7$ ),<sup>22–28</sup> as it is a crucial intermediate material used for the commercial production of high-purity Ta metal.<sup>29–32</sup> For example, Fordyce and Baum examined the infrared (IR) reflection spectra of niobium- and Ta-containing fluoride melts. They compared these spectra with those obtained for solid phases with a known structure and reported that heptafluorotantalate ( $TaF_7^{2-}$ ) and heptafluoronioabate were present in the corresponding melts.<sup>23</sup> Agulyanskii et al. obtained the same findings in their investigation of the IR emission spectra of the thick layers of melts.<sup>24</sup> In addition, they found that with an increase in temperature, the only discernible band shifted slightly toward

Received: September 19, 2023

Revised: October 29, 2023

Accepted: December 7, 2023

Published: December 27, 2023



higher wavenumbers. This high-frequency shift, which accompanied melting, was associated with changes in distances between the central atom and the first and second coordination spheres.<sup>33</sup> Kolosov et al. used potassium bromide to press a fine powder of  $K_2TaF_7$  into pellets to measure the IR spectra of  $K_2TaF_7$  under heat treatment at different temperatures.<sup>22</sup>

Although the aforementioned experiments and spectral studies have been conducted on  $K_2TaF_7$ , only some peaks in its IR and Raman spectra have been assigned to their corresponding vibrational modes. Moreover, there is a lack of theoretical methods for assigning peaks in these spectra to the appropriate vibrational modes. Therefore, in this study, we simulated the vibrational spectrum of  $K_2TaF_7$ , and used the normal mode to determine the distribution of related peaks and identify the vibrational mode of each peak obtained in the previously reported experiments.

## II. METHODS

A primitive cell of the  $K_2TaF_7$  crystal contains four molecules.<sup>25</sup> On the basis of first-principles density functional theory (DFT) simulations, we performed geometric optimization and phonon calculations using the Cambridge Serial Total Energy Package (CASTEP) code.<sup>33</sup> Considering that electron density fluctuates substantially in the  $K_2TaF_7$  crystal, we employed the generalized gradient approximation (GGA) of Perdew–Burke–Ernzerhof (PBE) exchange correlation functional.<sup>34</sup> The convergence tolerance of the self-consistent field (SCF) and ground energy were both set to  $1 \times 10^{-10}$  eV/atom. The  $k$ -point mesh was  $2 \times 1 \times 2$ , and the energy cutoff was set to 930 eV. A linear response approach was used to calculate IR and Raman intensities by using norm-conserving pseudopotentials. According to the IR calculation, we analyzed the dynamic process of normal modes at the gamma point and assigned peaks in simulated IR and Raman spectra to their corresponding vibrations. This enabled us to assign the peaks in the previously reported experimental IR and Raman spectra and identify those representing the highest absorbing Ta-related vibrations in terms of their photon–phonon resonance absorption (PPRA).

## III. RESULTS AND DISCUSSION

The space group of  $K_2TaF_7$  crystals is monoclinic  $P2_1/c$  with lattice parameters  $a = 5.8559$ ,  $b = 12.708$ ,  $c = 8.5125$  Å, and  $\beta = 90.17^\circ$ .<sup>35</sup>  $TaF_7^{2-}$  is formed as a trigonal prism with six of its fluorine atoms positioned in the prism's vertices. The seventh fluorine atom is positioned above the center of the rectangular face of the prism,<sup>36</sup> resulting in  $C_{2v}$  symmetry. On the harmonic approximation, we calculated vibrational modes at the gamma point to assign experimental peaks to particular vibrations.  $K_2TaF_7$  is a salt in which a light cation is associated with a heavy complex anion, which means that the frequency differences between some of the internal modes and external modes are small, such that they are symmetrically matched and can undergo coupling.<sup>25</sup> We classified all of the vibrational modes into four groups: rotation, translation, bending, and stretching.

The experimental<sup>25,27</sup> and calculated IR and Raman spectra are presented in Figure 1. A total of  $40 \times 3 - 3 = 117$  optical vibrational modes were identified for a 40-atom primitive cell.  $K_2TaF_7$  has a symmetric center, so changes in its dipole moment and polarizability are mutually exclusive after photon

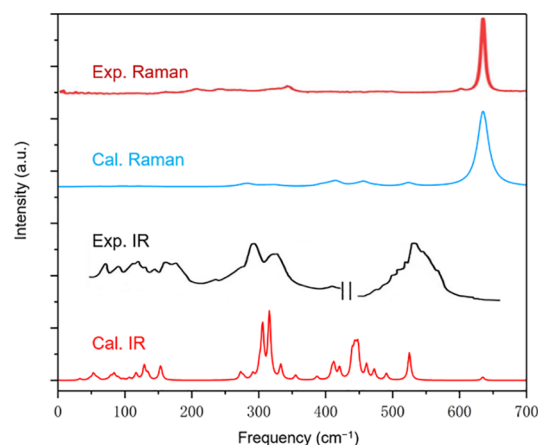


**Figure 1.** Comparison of experimental (Exp.) and calculated (Cal.) Raman and infrared (IR) spectra. Note that some data between 400 and 500  $cm^{-1}$  are missing from the Exp. IR spectrum.

absorption. Thus, as shown in Table 1, the IR and Raman active modes are fully complementary.

In the Raman spectrum (Figure 1), many lower bands were considerably broad, and some were ill-defined. This absence of features in the low-frequency Raman spectrum indicates the presence of compounds containing reorientated or disordered groups.<sup>25</sup> As presented in Table 1, fewer experimental data were collected from the low-frequency domain. Regardless of the intensities of the simulated spectra, all of the IR- or Raman-active modes are listed in Table 1. In the lowest region, the vibrational modes exhibited skeletal translation or rotation. Three IR-active modes were observed (at 33, 35, and 43  $cm^{-1}$ ), and four Raman-active modes were observed (at 35, 39, and 41(2)  $cm^{-1}$ ). Two degenerate modes were also observed at 41  $cm^{-1}$ . As shown in Figure 2, the Raman-active mode at 35  $cm^{-1}$  represents the skeletal translation of the potassium ion ( $K^+$ ) and the  $TaF_7^{2-}$  cluster along the  $z$ -axis. To keep the mass center static, two molecules vibrate in one direction, whereas another two molecules vibrate in the opposite direction. There are seven skeletal deformation modes in this region, and they are too weak to be experimentally detected.

English et al. examined the Raman scattering spectrum of  $TaF_7^{2-}$  in the rotational region and found medium-intensity vibration peaks at 60, 76, and 85  $cm^{-1}$ .<sup>25</sup> As shown in Table 1, these three peaks correspond to normal modes at 58, 76, and 86  $cm^{-1}$ , respectively. The authors detected only one IR peak in this region, at 63  $cm^{-1}$ . One example of the rotational mode at 76  $cm^{-1}$  is presented in Figure 2.

The findings of dynamics analysis indicated that the region from 94 to 163  $cm^{-1}$  is the translation band of  $K^+$ . Heys observed few peaks in this region and attributed a medium-intensity IR peak at 159  $cm^{-1}$  to the  $\nu_7$  mode.<sup>26</sup> English et al. observed more peaks at 300 K:<sup>25</sup> a prominent single peak at 106  $cm^{-1}$ ; and double peaks at 150 and 160  $cm^{-1}$ , corresponding to normal modes at 134 and 153  $cm^{-1}$ , respectively. In the current study, the simulated peaks exhibited a clear red shift, as the IR spectrum was calculated at 0 K, and a temperature reduction results in a slight red shift. Figure 2 depicts the translational mode of two  $K^+$ , as represented by the Raman-active mode at 117  $cm^{-1}$ .

We attributed the band from 282 to 479  $cm^{-1}$  to the bending vibrations of  $TaF_7^{2-}$ . Fordyce et al. reported that the mass of a cation has very little effect on the frequencies of

**Table 1. Comparison of Calculated Raman- or Infrared (IR)-Active Normal Modes for  $K_2TaF_7$  with Experimental Data (Unit:  $cm^{-1}$ ), Where “(2)” Indicates Two Degenerate Modes**

Normal modes	Active	IR exp.	Raman exp.	Vibrational modes
33	IR			skeletal rotation
35	Raman			skeletal translation
39	Raman			skeletal translation
41 (2)	Raman			skeletal translation
43	IR			skeletal rotation
48	IR			skeletal rotation
53	IR	63 <sup>a</sup>		TaF <sub>7</sub> <sup>2-</sup> rotation
53 (2)	Raman			TaF <sub>7</sub> <sup>2-</sup> rotation
56	IR			TaF <sub>7</sub> <sup>2-</sup> rotation
58	Raman		60 <sup>a</sup>	TaF <sub>7</sub> <sup>2-</sup> rotation
60	IR			TaF <sub>7</sub> <sup>2-</sup> rotation
60	Raman			TaF <sub>7</sub> <sup>2-</sup> rotation
63	Raman			TaF <sub>7</sub> <sup>2-</sup> rotation
67	Raman			TaF <sub>7</sub> <sup>2-</sup> rotation
68	IR			TaF <sub>7</sub> <sup>2-</sup> rotation
74 (2)	IR			TaF <sub>7</sub> <sup>2-</sup> rotation
76	Raman		76 <sup>a</sup>	TaF <sub>7</sub> <sup>2-</sup> rotation
77	Raman			TaF <sub>7</sub> <sup>2-</sup> rotation
78	IR			TaF <sub>7</sub> <sup>2-</sup> rotation
79	Raman			TaF <sub>7</sub> <sup>2-</sup> rotation
79	IR			TaF <sub>7</sub> <sup>2-</sup> rotation
84 (2)	IR			TaF <sub>7</sub> <sup>2-</sup> rotation
86	Raman		85 <sup>a</sup>	TaF <sub>7</sub> <sup>2-</sup> rotation
90	IR			TaF <sub>7</sub> <sup>2-</sup> rotation
91	Raman			TaF <sub>7</sub> <sup>2-</sup> rotation
94	Raman			K <sup>+</sup> translation
96 (2)	Raman			K <sup>+</sup> translation
97	IR			K <sup>+</sup> translation
104	Raman		103 <sup>a</sup>	K <sup>+</sup> translation
107 (2)	IR	~106 <sup>a</sup>		K <sup>+</sup> translation
107	Raman			K <sup>+</sup> translation
117	IR	114 <sup>a</sup>		K <sup>+</sup> translation
117	Raman		114 <sup>a</sup>	K <sup>+</sup> translation
120	IR			K <sup>+</sup> translation
121	Raman		121 <sup>a</sup>	K <sup>+</sup> translation
125	Raman			K <sup>+</sup> translation
127	Raman		126 <sup>a</sup>	K <sup>+</sup> translation
129 (2)	IR	139 <sup>a</sup>		K <sup>+</sup> translation
134	Raman			K <sup>+</sup> translation
134	IR	150 <sup>a</sup>		K <sup>+</sup> translation
135	Raman		141 <sup>a</sup>	K <sup>+</sup> translation
145	Raman		150 <sup>a</sup>	K <sup>+</sup> translation
148	IR			K <sup>+</sup> translation
153	IR	160 <sup>a</sup> , 159 <sup>b</sup>		K <sup>+</sup> translation
154	IR			K <sup>+</sup> translation
163	Raman		156 <sup>a</sup>	K <sup>+</sup> translation
258 (2)	IR			TaF <sub>7</sub> <sup>2-</sup> bending
265	Raman		262 <sup>a</sup>	TaF <sub>7</sub> <sup>2-</sup> bending
266	Raman			TaF <sub>7</sub> <sup>2-</sup> bending
273	IR	~260 <sup>a</sup> , 265 <sup>c</sup>		TaF <sub>7</sub> <sup>2-</sup> bending
273	Raman		272 <sup>a</sup> , 276 <sup>d</sup>	TaF <sub>7</sub> <sup>2-</sup> bending
277	IR			TaF <sub>7</sub> <sup>2-</sup> bending
283	Raman			TaF <sub>7</sub> <sup>2-</sup> bending
291	IR			TaF <sub>7</sub> <sup>2-</sup> bending
294	Raman		292 <sup>a</sup>	TaF <sub>7</sub> <sup>2-</sup> bending
301	IR			TaF <sub>7</sub> <sup>2-</sup> bending
305	Raman		305 <sup>a</sup> , 306 <sup>d</sup>	TaF <sub>7</sub> <sup>2-</sup> bending
305 (2)	IR	279 <sup>a</sup> , 285 <sup>c</sup>		TaF <sub>7</sub> <sup>2-</sup> bending
311 (2)	Raman			TaF <sub>7</sub> <sup>2-</sup> bending
315	IR			TaF <sub>7</sub> <sup>2-</sup> bending

Table 1. continued

Normal modes	Active	IR exp.	Raman exp.	Vibrational modes
316	IR	309 <sup>a</sup> , 315 <sup>c</sup>		TaF <sub>7</sub> <sup>2-</sup> bending
320	IR			TaF <sub>7</sub> <sup>2-</sup> bending
323	Raman		320 <sup>at</sup>	TaF <sub>7</sub> <sup>2-</sup> bending
325	Raman			TaF <sub>7</sub> <sup>2-</sup> bending
332	Raman		326 <sup>a</sup> , 330 <sup>at</sup>	TaF <sub>7</sub> <sup>2-</sup> bending
333	IR			TaF <sub>7</sub> <sup>2-</sup> bending
337	Raman		334 <sup>at</sup>	TaF <sub>7</sub> <sup>2-</sup> bending
343	Raman		342 <sup>at</sup>	TaF <sub>7</sub> <sup>2-</sup> bending
346	IR			TaF <sub>7</sub> <sup>2-</sup> bending
355	IR			TaF <sub>7</sub> <sup>2-</sup> bending
357	Raman			TaF <sub>7</sub> <sup>2-</sup> bending
385	IR			TaF <sub>7</sub> <sup>2-</sup> bending
387	IR			TaF <sub>7</sub> <sup>2-</sup> bending
394 (2)	Raman		377 <sup>a</sup> , 373 <sup>at</sup>	TaF <sub>7</sub> <sup>2-</sup> bending
407	Raman			TaF <sub>7</sub> <sup>2-</sup> bending
409	IR			TaF <sub>7</sub> <sup>2-</sup> bending
412	IR	~400 <sup>at</sup>		TaF <sub>7</sub> <sup>2-</sup> bending
413	IR			TaF <sub>7</sub> <sup>2-</sup> bending
414	Raman		390 <sup>a</sup> , 392 <sup>at</sup>	TaF <sub>7</sub> <sup>2-</sup> bending
417 (2)	Raman			TaF <sub>7</sub> <sup>2-</sup> bending
421	IR			TaF <sub>7</sub> <sup>2-</sup> bending
439	IR			TaF <sub>7</sub> <sup>2-</sup> bending
441	Raman		444 <sup>at</sup>	TaF <sub>7</sub> <sup>2-</sup> bending
443	IR			TaF <sub>7</sub> <sup>2-</sup> bending
446	IR			TaF <sub>7</sub> <sup>2-</sup> bending
447	Raman			TaF <sub>7</sub> <sup>2-</sup> bending
448	IR			TaF <sub>7</sub> <sup>2-</sup> bending
450	Raman		452 <sup>at</sup>	TaF <sub>7</sub> <sup>2-</sup> bending
457 (2)	Raman			TaF <sub>7</sub> <sup>2-</sup> bending
461	IR	485 <sup>at</sup>		TaF <sub>7</sub> <sup>2-</sup> bending
472	IR			TaF <sub>7</sub> <sup>2-</sup> bending
473	Raman			TaF <sub>7</sub> <sup>2-</sup> bending
476	IR			TaF <sub>7</sub> <sup>2-</sup> bending
479	Raman			TaF <sub>7</sub> <sup>2-</sup> bending
491	IR	500 <sup>at</sup>		TaF <sub>7</sub> <sup>2-</sup> stretching
502	Raman		507 <sup>at</sup>	TaF <sub>7</sub> <sup>2-</sup> stretching
524	Raman		525 <sup>at</sup>	TaF <sub>7</sub> <sup>2-</sup> stretching
525	IR	530 <sup>a</sup> , 535 <sup>c</sup> , 530 <sup>e</sup>		TaF <sub>7</sub> <sup>2-</sup> stretching
531	IR	545 <sup>at</sup>		TaF <sub>7</sub> <sup>2-</sup> stretching
531	Raman		530 <sup>at</sup>	TaF <sub>7</sub> <sup>2-</sup> stretching
635	Raman		639 <sup>a</sup> , 640 <sup>at</sup>	TaF <sub>7</sub> <sup>2-</sup> stretching
635 (2)	IR	640 <sup>a</sup> , 641 <sup>c</sup> , 642 <sup>e</sup>		TaF <sub>7</sub> <sup>2-</sup> stretching
636	Raman			TaF <sub>7</sub> <sup>2-</sup> stretching

<sup>a</sup>Reference 25. <sup>b</sup>Reference 26. <sup>c</sup>Reference 23. <sup>d</sup>Reference 27. <sup>e</sup>Reference 22.

internal vibrations of complex anions. They noticed a medium intensity band at 265 cm<sup>-1</sup> and considerably high-intensity split bands at 285 and 315 cm<sup>-1</sup> in the IR spectra of TaF<sub>7</sub><sup>2-</sup>.<sup>23</sup> Furthermore, English et al. found a medium-intensity peak close to 260 cm<sup>-1</sup> and two sharp peaks at 279 and 309 cm<sup>-1</sup> in the IR spectrum of TaF<sub>7</sub><sup>2-</sup>.<sup>25</sup> As shown in Table 1, these three peaks correspond to normal modes at 272, 305 (2), and 316 cm<sup>-1</sup>, respectively. The two sharp simulated IR peaks at 305 and 316 cm<sup>-1</sup> are shown in Figure 1. Figure 2 presents the vibrational mode at 316 cm<sup>-1</sup>, and details regarding the dynamic process are provided in the Supporting Information file. Because these two peaks represent highly efficient IR absorption, we selected them as candidates for PPRA. Although many Raman peaks were collected from experiments

in this band, their intensities were very low, as shown in (Figure 1).

The last band comprised the stretching modes of TaF<sub>7</sub><sup>2-</sup>. Kolosov hypothesized that IR peaks at 530 and 642 cm<sup>-1</sup>, which correspond to the asymmetric and symmetric stretching modes of TaF<sub>7</sub><sup>2-</sup>,<sup>22</sup> constitute the major absorption peaks in the high-frequency region. Agulyansky assigned the IR peak at 530 cm<sup>-1</sup> and the Raman peak at 639 cm<sup>-1</sup> to the asymmetric stretching modes of TaF<sub>7</sub><sup>2-</sup>.<sup>32</sup> Fordyce identified a sharp IR band at 535 cm<sup>-1</sup> and a weak IR band at 641 cm<sup>-1</sup>. They indicated that a completely symmetrical vibration was the most likely cause of the weak IR peak at 641 cm<sup>-1</sup>. However, English et al. assigned the intense Raman peak at 639 cm<sup>-1</sup> to the asymmetric stretching mode and the IR peak at 530 cm<sup>-1</sup> to the symmetric stretching mode. The results of dynamics

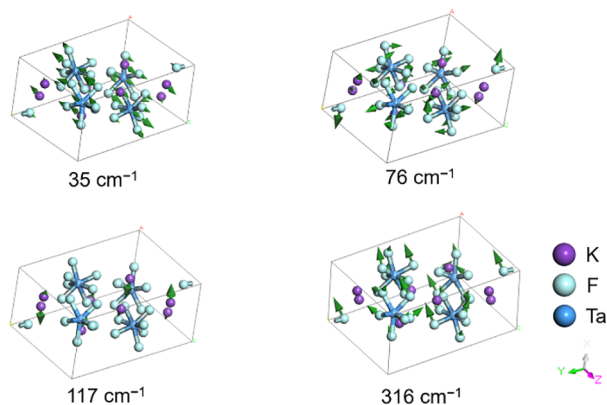


**Figure 2.** Four examples of vibrational modes in the lowest region. The green arrows indicate the direction of the vibration, which is proportional to the amplitude.

analysis performed in this study reveal that the IR-active mode at  $525\text{ cm}^{-1}$  and the Raman-active mode at  $531\text{ cm}^{-1}$  reflect Ta–F asymmetric stretching, whereas the IR- and Raman-active modes at  $635\text{ cm}^{-1}$  represent the two types of Ta–F symmetric stretching.

In summary, the experimentally observed IR peak at approximately  $525\text{ cm}^{-1}$  and the Raman peak at approximately  $635\text{ cm}^{-1}$  can be attributed to asymmetric and symmetric stretching, respectively. Figure 3 presents these four stretching

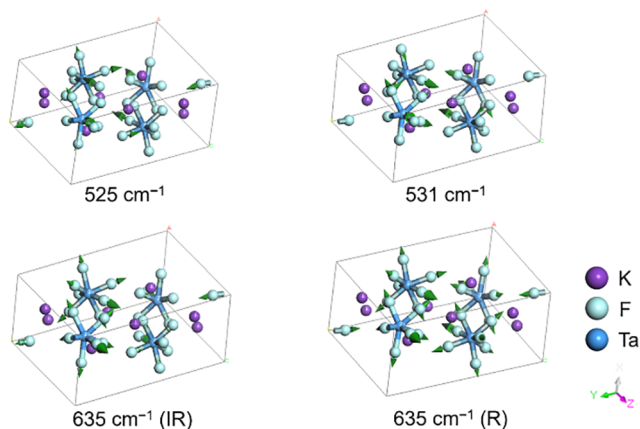


**Figure 3.** Four stretching modes of the heptafluorotantalate ion ( $\text{TaF}_7^{2-}$ ). Asymmetric stretching is exhibited by the modes at  $525$  and  $531\text{ cm}^{-1}$ , respectively, whereas symmetric stretching is exhibited by the two modes at  $635\text{ cm}^{-1}$ . The modes at  $635\text{ cm}^{-1}$  are infrared (IR)- and Raman (R)-active, respectively.

modes. Details regarding the dynamic process of the IR-active mode at  $525\text{ cm}^{-1}$  are provided in the Supporting Information file. Thus, the IR active mode at  $525\text{ cm}^{-1}$  is an ideal candidate for PPRA analysis.

#### IV. CONCLUSION

On the basis of first-principle DFT simulations, we analyzed the vibrational normal modes of  $\text{K}_2\text{TaF}_7$ . Most of the vibrational modes of  $\text{K}^+$  and  $\text{TaF}_7^{2-}$  vibrated independently. According to the results of dynamics analysis, we classified the vibrational modes and compared some of these with previously reported experimental data.

From the perspective of the photothermal effect, the most efficient method is resonance absorption. However, photon–phonon coupling intensities are limited by selection rules. Therefore, in this study, we identified Ta-related strong absorption peaks. We found that the peaks at  $305$  and  $316\text{ cm}^{-1}$  in the calculated IR spectrum correspond to the experimentally detected peaks at  $285$  and  $315\text{ cm}^{-1}$ , respectively. These two peaks are related to the Ta rotation. The peak at approximately  $530\text{ cm}^{-1}$  in the experimental IR spectrum corresponds to the Ta–F stretching mode. Finally, we selected three IR absorption peaks at  $285$ ,  $315$ , and  $530\text{ cm}^{-1}$ . We hypothesize that subjecting  $\text{K}_2\text{TaF}_7$  to high-power terahertz (THz) laser radiation targeting the vibrational modes represented by these three absorption peaks (i.e.,  $8.55$ -,  $9.45$ -, and  $15.9$ -THz radiation, respectively) will produce a marked photothermal effect that will facilitate the separation of Ta from  $\text{K}_2\text{TaF}_7$ , thereby improving the production efficiency of the tantalum preparation plant. Currently, terahertz free-electron lasers (FELs) face challenges in terms of cost and limited frequency bands. Nevertheless, as these frequency bands are expanded, the distinctive frequency selection advantages of terahertz FELs hold promise for aiding in the separation of tantalum by leveraging tantalum-related strong absorption peaks.

#### ■ ASSOCIATED CONTENT

##### Supporting Information

The Supporting Information is available free of charge at <https://pubs.acs.org/doi/10.1021/acsomega.3c07117>.

IR vibrational mode at  $316\text{ cm}^{-1}$  (MP4)

IR vibrational mode at  $525\text{ cm}^{-1}$  (MP4)

#### ■ AUTHOR INFORMATION

##### Corresponding Author

Peng Zhang – School of Space Science and Physics, Shandong University, Weihai 264209, China; [orcid.org/0000-0002-1099-6310](https://orcid.org/0000-0002-1099-6310); Email: [zhangpeng@sdu.edu.cn](mailto:zhangpeng@sdu.edu.cn)

##### Authors

Yi-Ning Li – School of Space Science and Physics, Shandong University, Weihai 264209, China

Qing Guo – School of Space Science and Physics, Shandong University, Weihai 264209, China

Si-Cheng Liu – School of Space Science and Physics, Shandong University, Weihai 264209, China

Xiao-Yan Liu – School of Space Science and Physics, Shandong University, Weihai 264209, China

Yan Jiang – School of Space Science and Physics, Shandong University, Weihai 264209, China

Yi Yin – School of Space Science and Physics, Shandong University, Weihai 264209, China

Complete contact information is available at:

<https://pubs.acs.org/doi/10.1021/acsomega.3c07117>

##### Notes

The authors declare no competing financial interest.

#### ■ ACKNOWLEDGMENTS

We are grateful to the project ZR2022MA017 supported by Shandong Provincial Natural Science for financial support. The numerical calculations were performed on the supercomputing

system at the Supercomputing Center, Shandong University, Weihai.

## REFERENCES

- (1) de Souza, K. A.; Robin, A. Influence of concentration and temperature on the corrosion behavior of titanium, titanium-20 and 40% tantalum alloys and tantalum in sulfuric acid solutions. *Mater. Chem. Phys.* **2007**, *103*, 351–360.
- (2) Breznay, N. P.; Tendulkar, M.; Zhang, L.; Lee, S. C.; Kapitulnik, A. Superconductor to weak-insulator transitions in disordered tantalum nitride films. *Phys. Rev. B* **2017**, *96*, No. 134522.
- (3) Castro, R. G.; Smith, R. W.; Rollett, A. D.; Stanek, P. W. Toughness of dense mosi2 and mosi2tantalum composites produced by low pressure plasma deposition. *Scripta Metallurgica Et Materialia* **1992**, *26*, 207–212.
- (4) TSUBONE, I.; NAKAJIMA, Y.; KANDA, Y. Resonance Parameters of Tantalum-181 in Neutron Energy Range from 100 to 4,300eV. *J. NUCL SCI TECHNOL* **1987**, *24*, 975–987.
- (5) Hwang, S. M.; Park, S. J.; Wang, J. P.; Park, Y. H.; Lee, D. W. Preparation of tantalum metal powder by magnesium gas reduction of tantalum pentoxide with different initial particle size. *Int. J. Refract. Met. Hard Mater.* **2021**, *100*, No. 105620.
- (6) Wu, T.; Jin, X.; Xiao, W.; Hu, X.; Wang, D.; Chen, G. Z. Thin Pellets: Fast Electrochemical Preparation of Capacitor Tantalum Powders. *Chem. Mater.* **2007**, *19*, 153–160.
- (7) Matsuno, H.; Yokoyama, A.; Watari, F.; Uo, M.; Kawasaki, T. Biocompatibility and osteogenesis of refractory metal implants, titanium, hafnium, niobium, tantalum and rhenium. *Biomaterials* **2001**, *22*, 1253–1262.
- (8) Cheng, Y.; Cai, W.; Li, H. T.; Zheng, Y. F. Surface modification of NiTi alloy with tantalum to improve its biocompatibility and radiopacity. *J. Mater. Sci.* **2006**, *41*, 4961–4964.
- (9) Balla, V. K.; Bose, S.; Davies, N. M.; Bandyopadhyay, A. Tantalum—A bioactive metal for implants. *JOM* **2010**, *62*, 61–64.
- (10) Adamek, G. Tantalum foams prepared by the thermal dealloying process. *Int. J. Refract. Met. Hard Mater.* **2017**, *65*, 88–93.
- (11) Uslu, E.; Oztatli, H.; Garipcan, B.; Ercan, B. Fabrication and cellular interactions of nanoporous tantalum oxide. *J. Biomed. Mater. Res. Part B* **2020**, *108*, 2743–2753.
- (12) Hwang, S. M.; Wang, J. P.; Lee, D. W. Extraction of Tantalum Powder via the Magnesium Reduction of Tantalum Pentoxide. *Metals* **2019**, *9*, 205.
- (13) Nersisyan, H.; Ryu, H. S.; Lee, J. H.; Suh, H.; Won, H. I. Tantalum network nanoparticles from a Ta<sub>2</sub>O<sub>5</sub>+kMg system by liquid magnesium controlled combustion. *Combust. Flame* **2020**, *219*, 136–146.
- (14) Kolosov, V. N.; Miroshnichenko, M. N.; Orlov, V. M.; Prokhorova, T. Y. Sodium Thermal Reduction of Tantalum Powders from Melts with Tantalum Pentoxide Additions. *Russ. Metall. (Engl. Transl.)* **2009**, *2009*, 473–477.
- (15) Prokhorova, T. Y.; Orlov, V. M.; Miroshnichenko, M. N.; Kolosov, V. N. Effect of the Conditions of Sintering of Sodium-Reduced Tantalum Powders on Their Characteristics. *Russ. Metall. (Engl. Transl.)* **2014**, *2014*, 576–580.
- (16) Grinevitch, V.V.; Kuznetsov, S.A.; Arakcheeva, A.A.; Olyunina, T.V.; Schonleber, A.; Gaune-Escard, M. Electrode and chemical reactions during electrodeposition of tantalum products in CsCl melt. *Electrochim. Acta* **2006**, *51*, 6563–6571.
- (17) Mais, L. *Electrodeposition of Nb, Ta, Zr and Cu from Ionic Liquid for Nanocomposites Preparation*. PhD thesis, University of Cagliari: Italy, 2015.
- (18) Purushotham, Y.; Ravindranath, K.; Kumar, A.; Govindaiah, R. M.; Prakash, T. L. Quality improvements in tantalum powder by automation of sodium reduction system. *International Journal of Refractory Metals and Hard Materials. Int. J. Refract. Met. Hard Mater.* **2009**, *27*, 571–576.
- (19) Mizusaki, Y.; Iijima, H.; Noguchi, Y. Tantalum powder and methods of manufacturing same. US7679885B2, 2008.
- (20) Kolosov, V. N.; Miroshnichenko, M. N.; Prokhorova, T. Y.; Orlov, V. M. Preparation of tantalum powders by the reduction of complex oxyfluoride compounds with sodium. *RUSS. J. NON-FERR. MET* **2016**, *57*, 599–603.
- (21) Wilkes, J. S. A short history of ionic liquids—from molten salts to neoteric solvents. *Green Chem.* **2002**, *4*, 73–80.
- (22) Kolosov, V. N.; Orlov, V. M.; Miroshnichenko, M. N.; Prokhorova, T. Y. Preparation of tantalum powders via the sodium reduction of potassium heptafluorotantalate heat-treated in air. *Inorg. Mater.* **2015**, *51*, 116–121.
- (23) Fordyce, J. S.; Baum, R. L. Infrared-Reflection Spectra of Molten Fluoride Solutions: Tantalum (V) in Alkali Fluorides. *J. Chem. Phys.* **1966**, *44*, 1159–1165.
- (24) Agulyanskii, A. I.; Sakharov, Y. A. Experimental unit for measuring infrared emission spectra of molten salts. *J. Appl. Spectrosc.* **1979**, *31*, 1007–1009.
- (25) English, R. B.; Heyns, A. M.; Reynhardt, E. C. An X-ray, NMR, infrared and Raman study of K<sub>2</sub>TaF<sub>7</sub>. *J. Phys. C: Solid State Phys.* **1983**, *16*, 829–840.
- (26) Heyns, A. M. The vibrational spectra of crystals of K<sub>2</sub>TaF<sub>7</sub>. *J. Mol. Struct.* **1982**, *79*, 391–394.
- (27) Liu, X. Y.; Wang, B. Z.; Fu, H. Y.; Wang, C. Y. Raman spectroscopic and theoretical studies on the structure of Ta (V) fluoro and oxofluoro complexes in molten FLiNaK. *J. Mol. Liq.* **2021**, *337*, No. 116409.
- (28) Zalkind, O. A.; Kolosov, V. N.; Matychenko, E. S.; Orlov, V. M. Determination of Oxygen in Halide Fluorotantalate Melts by IR Spectroscopy. *J. Anal. Chem.* **2001**, *56*, 1020–1021.
- (29) Kolosov, V. N.; Orlov, V. M.; Miroshnichenko, M. N.; Prokhorova, T. Y. Preparation of high-purity tantalum powders by sodium-thermal reduction. *Inorg. Mater.* **2012**, *48*, 903–907.
- (30) Luo, G. Q.; Li, H.; Chen, X. Q.; Wang, X. M. Effect of Potassium Fluorotantalate Reduction Condition on Properties of Tantalum Powder. *Youse Jinshu (Yelian Bufen)* **2022**, *11*, 85–88.
- (31) Agulyansky, A. *Chemistry of Tantalum and Niobium Fluoride Compounds*; Elsevier: Amsterdam, 2004; pp 407.
- (32) Agulyansky, A. Potassium fluorotantalate in solid, dissolved and molten conditions. *J. Fluorine Chem.* **2003**, *123*, 155–161.
- (33) Clark, S. J.; Segall, M. D.; Pickard, C. J.; Hasnip, P. J.; Probert, M. J.; Refson, K.; Payne, M. C. First principles methods using CASTEP. *Z. Kristallogr. – Cryst. Mater.* **2005**, *220*, 567–570.
- (34) Perdew, J. P.; Burke, K.; Ernzerhof, M. Generalized Gradient Approximation Made Simple. *Phys. Rev. Lett.* **1996**, *77*, 3865–3868.
- (35) Torardi, C. C.; Brixner, L. H.; Blasse, G. Structure and luminescence of K<sub>2</sub>TaF<sub>7</sub> and K<sub>2</sub>NbF<sub>7</sub>. *J. Solid State Chem.* **1987**, *67*, 21–25.
- (36) Hoard, J. L. Structures of Complex Fluorides. I Potassium Heptafluorocolumbate and Potassium Heptafluorotantalate. The Configuration of the Heptafluorocolumbate and Heptafluorotantalate Ions. *J. Am. Chem. Soc.* **1939**, *61*, 1252–1259.